Supplemental Materials

Molecular Biology of the Cell

Gou et al.

Supplementary Material for: Mathematical model with spatially uniform regulation explains long-range bidirectional transport of early endosomes in fungal hyphae

Jia Gou, Leah Edelstein-Keshet, Jun Allard

Contents

1 Geometry and conventions

Throughout the model derivations, we consider a 1D cell with length L. We describe densities in terms of a single spatial variable $0 \leq x \leq L$. We denote $x = L$ as the "right" and $x = 0$ as the "left" cell end. A microtubule considered to "face right" if it is oriented with plus end towards $x = L$ and minus end towards $x = 0$. Similarly, we describe motors moving right or left according to their direction to $x = L$ or $x = 0$.

2 Microtubule Distribution Model

We model the assembly and disassembly of microtubules (MT) by tracking the growth and catastrophe of their plus ends. We assume that minus ends are trapped in gamma-tubulin ring complexes distributed through the hyphae and neither grow nor shrink. The number of right-facing, growing MTs with plus-ends in $(x^p, x^p + dx)$ and minus-ends in $(x^m, x^m + dx)$ is denoted $\rho_g^R(x^p, x^m, t)dx^m dx^p$.

The dynamics of MT growth and shrinkage can be described by the Dogterom-Leibler equations (1).

$$\begin{cases} \dfrac{\partial \rho_g^R}{\partial t} = -v_g \dfrac{\partial \rho_g^R}{\partial x^p} - k_c \rho_g^R + k_r \rho_s^R, \\ \dfrac{\partial \rho_s^R}{\partial t} = +v_s \dfrac{\partial \rho_s^R}{\partial x^p} + k_c \rho_g^R - k_r \rho_s^R, \end{cases}$$

$$\begin{cases} \dfrac{\partial \rho_g^L}{\partial t} = +v_g \dfrac{\partial \rho_g^L}{\partial x^p} - k_c \rho_g^L + k_r \rho_s^L, \\ \dfrac{\partial \rho_s^L}{\partial t} = -v_s \dfrac{\partial \rho_s^L}{\partial x^p} + k_c \rho_g^L - k_r \rho_s^L, \end{cases}$$

where v_g, v_s are growth and shrinkage velocities, k_c, k_r rates of catastrophe and rescue of MT ends.

We assume equal nucleation probability for both directions, so that MT are spawned (with new pointed ends coinciding with the minus end location at gamma-tubulin ring complexes) growing to left and right with equal nucleation rates ($k_{nuc}/2$). This implies that

$$+v_g \rho_g^R(x^p, x^p, t) = \frac{k_{nuc}}{2}, \quad -v_g \rho_g^L(x^p, x^p, t) = \frac{k_{nuc}}{2}.$$

Let l_{nuc} represents the size of the tip region. Then, since no new MTs are nucleated at either cell tip or septum, we assume that k_{nuc} depends on the location as follows:

$$k_{nuc} = \begin{cases} k_{nuc}^0, & x^m \in (l_{nuc}, L - l_{nuc}), \\ 0, & \text{otherwise.} \end{cases}$$

While the value of the parameter k^0_{nuc} affects the MT and plus ends solutions, it does not affect the ratio of right and left facing MT (nor the plus ends ratio). Thus, as we show later, this parameter does not affect the dynein or endosome distributions that we obtain in our models (discussed below).

At the ends of the cell, we assume that the flux of arriving MT ends is balanced by flux of MT ends shrinking away. This ensures that MT tips do not disappear at the cell ends and results in the boundary conditions (at $x = 0, L$),

$$\begin{aligned} v_g\rho^R_g(L, x^m, t) &= v_s\rho^R_s(L, x^m, t), \\ v_g\rho^L_g(0, x^m, t) &= v_s\rho^L_s(0, x^m, t). \end{aligned}$$

The above system of equations is solved at steady state. From the resulting solutions we can obtain several experimentally measurable observables. First, we define the *array polarity in plus-end density* as follows. The density of right moving plus ends at x consists of all plus ends moving right whose minus ends are to the left of x, as depicted by the integral

$$p^R(x) = \int_0^x [\rho^R_g(x, x^m) + \rho^R_s(x, x^m)]dx^m. \quad [1]$$

Similarly the density of left moving plus ends at x is

$$p^L(x) = \int_x^L [\rho^L_g(x, x^m) + \rho^L_s(x, x^m)]dx^m. \quad [2]$$

The fraction, $p(x)$, of right moving plus ends at x is then

$$p(x) = \frac{p^R(x)}{p^R(x) + p^L(x)}.$$

We also obtain the *MT array polarity*. Let $N^R(x)$ be the total number of right-facing MTs in a cross-section at x. Such MT have minus ends "to the left" of x and plus ends "to the right" of x, so

$$N^R(x) = \int_x^L \int_0^x [\rho^R_g(x^p, x^m) + \rho^R_s(x^p, x^m)]dx^m dx^p. \quad [3]$$

Similarly, the total number of left-facing MTs, $N^L(x)$ is given by

$$N^L(x) = \int_x^L \int_0^x [\rho^L_g(x^p, x^m) + \rho^L_s(x^p, x^m)]dx^p dx^m. \quad [4]$$

The fraction, $P(x)$, of right facing MTs is then

$$P(x) = \frac{N^R(x)}{N^R(x) + N^L(x)}. \quad [5]$$

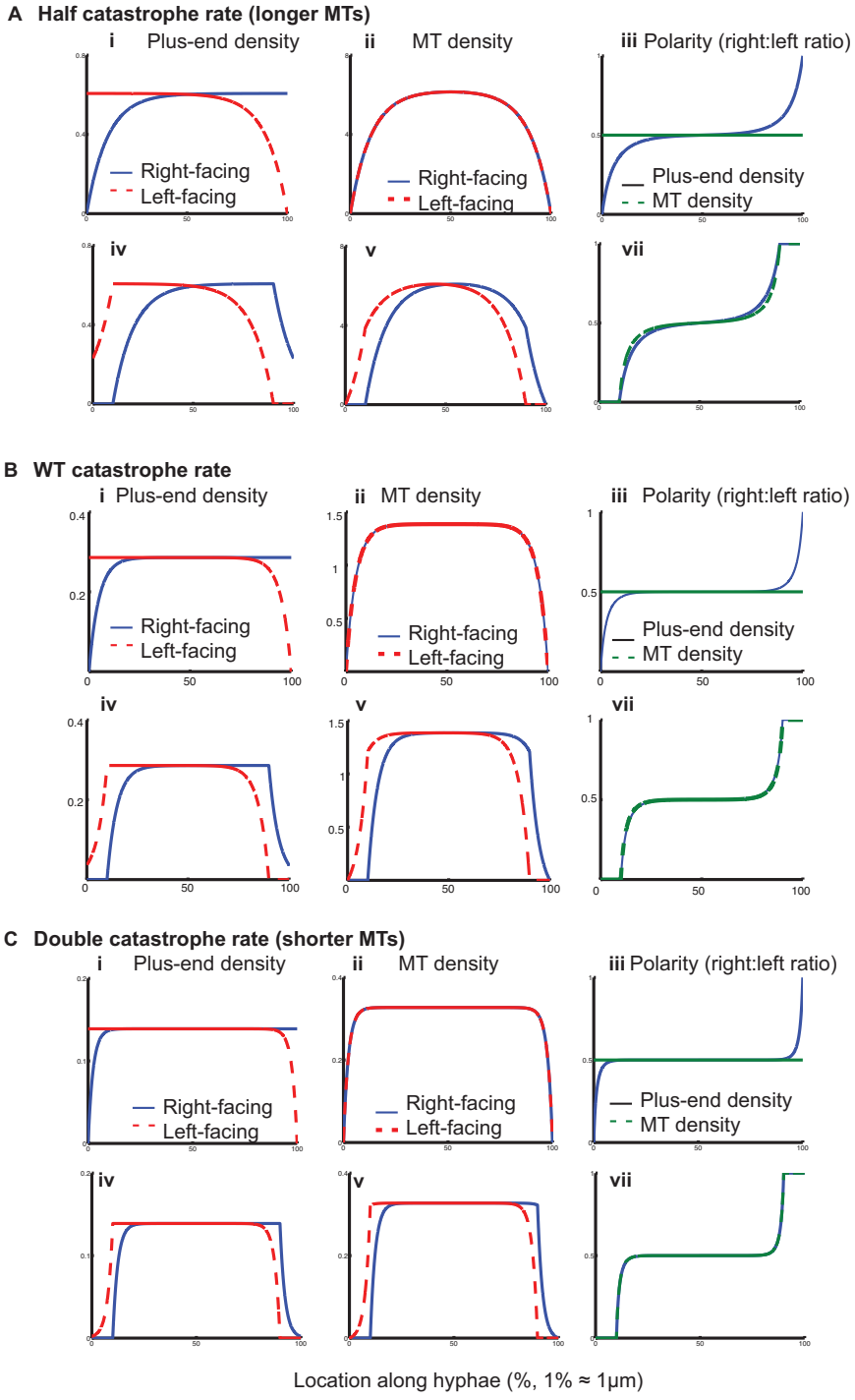

Figure 1: A comparison of results for MT distribution (Fig 2 of main text) for (A) shorter, (B) normal, and (C) longer microtubules. The catastrophe rate (k_c) was the only parameter adjusted for A,B,C.

As noted earlier, k^0_{nuc} affects N^R, N^L, p^R, p^L, but not the ratios $P(x), p(x)$. Only $P(x)$ is used later on in the dynein and endosome models. We solved the steady state system of MT equations and boundary conditions. The full solutions (not shown) led to the expressions for the functions N^R, N^L as follows:

$$N^R(x) = \begin{cases} 0, & 0 < x < l_{nuc} \\ \frac{k^0_{nuc}\lambda^2}{2}(\frac{1}{v_g}+\frac{1}{v_s})(1-e^{-\frac{L-x}{\lambda}})(1-e^{\frac{l_{nuc}-x}{\lambda}}), & l_{nuc} < x < L-l_{nuc}, \\ \frac{k^0_{nuc}\lambda^2}{2}(\frac{1}{v_g}+\frac{1}{v_s})e^{-\frac{x}{\lambda}}(1-e^{-\frac{L-x}{\lambda}})(e^{\frac{L-l_{nuc}}{\lambda}}-e^{\frac{l_{nuc}}{\lambda}}), & L-l_{nuc} < x < L, \end{cases}$$

$$N^L(x) = \begin{cases} \frac{k^0_{nuc}\lambda^2}{2}(\frac{1}{v_g}+\frac{1}{v_s})e^{\frac{x}{\lambda}}(1-e^{-\frac{x}{\lambda}})(e^{-\frac{l_{nuc}}{\lambda}}-e^{-\frac{L-l_{nuc}}{\lambda}}), & 0 < x < l_{nuc}, \\ \frac{k^0_{nuc}\lambda^2}{2}(\frac{1}{v_g}+\frac{1}{v_s})(1-e^{-\frac{L-l_{nuc}-x}{\lambda}})(1-e^{-\frac{x}{\lambda}}), & l_{nuc} < x < L-l_{nuc}, \\ 0, & L-l_{nuc} < x < L, \end{cases}$$

and the expressions for the plus and minus ends density $p^R(x), p^L(x)$ are

$$p^R(x) = \begin{cases} 0, & 0 < x < l_{nuc} \\ \frac{k^0_{nuc}\lambda}{2}(\frac{1}{v_g}+\frac{1}{v_s})(1-e^{\frac{l_{nuc}-x}{\lambda}}), & l_{nuc} < x < L-l_{nuc}, \\ \frac{k^0_{nuc}\lambda}{2}(\frac{1}{v_g}+\frac{1}{v_s})e^{\frac{-x}{\lambda}}(e^{\frac{L-l_{nuc}}{\lambda}}-e^{\frac{l_{nuc}}{\lambda}}), & L-l_{nuc} < x < L, \end{cases}$$

$$p^L(x) = \begin{cases} \frac{k^0_{nuc}\lambda}{2}(\frac{1}{v_g}+\frac{1}{v_s})e^{\frac{x}{\lambda}}(e^{-\frac{l_{nuc}}{\lambda}}-e^{-\frac{L-l_{nuc}}{\lambda}}), & 0 < x < l_{nuc}, \\ \frac{k^0_{nuc}\lambda}{2}(\frac{1}{v_g}+\frac{1}{v_s})e^{\frac{x}{\lambda}}(e^{-\frac{x}{\lambda}}-e^{-\frac{L-l_{nuc}}{\lambda}}), & l_{nuc} < x < L-l_{nuc}, \\ 0, & L-l_{nuc} < x < L, \end{cases}$$

where λ, the characteristic MT length, is

$$\lambda = \frac{v_g v_s}{k_c v_s - k_r v_g}. \qquad [6]$$

Based on typical MT parameters (see Table 1), the mean length of MT is $\lambda \approx 4.8\mu$m. Figure 2 in the main text shows (B, E) the distribution of right and left facing plus-end densities $p^R(x), p^L(x)$, (C, F) right and left facing MT densities $N^R(x)$, $N^L(x)$ and (D, G) the right:left ratios of plus ends $p(x)$ and of MT $P(x)$.

2.1 Shorter and longer microtubules

We asked how the predicted mean microtubule length of $\sim 5\mu$m affects our results. We explored this using faster or slower rates of catastrophe. Consequently, we simulated MT dynamics for both isotropic nucleation and inhibited end zones, as in Figure 2 of the main text, but for values of k_c that were (A) half (B) the same as, or (C) double the WT value. Results are shown in Fig. 1. We find that the qualitative results are insensitive to this perturbation in mean MT length: both the values of densities and polarities in the interior, as well as at $x = 0, L$ are highly similar. This suggests that the MT nucleation inhibition

zones are the primary determinant of the MT array pattern. We find some subtle changes: For larger k_c (smaller MT), the transition zones are sharper. This is intuitively clear, since, according to [6], the rate of spatial exponential decay $1/\lambda$ increases as k_c increases (with other parameters kept fixed), making the spatial transitions more abrupt.

3 Dynein Dynamics

In modeling dynein, we let $d^i(x,t)$ represent the density of dynein motors per μm of hyphal length. Dynein can either move freely (F) under its own power (towards the minus end of a MT) or it can be carried by a kinesin-1 (K) moving towards a plus MT end. (There is also a subpopulation of dynein being transported by kinesin-3 via attachment to an EE. We neglect a sixth subpopulation of dynein currently transporting EE.) Furthermore, in some but not all models, we consider the possibility of exchange with a cytoplasmic dynein pool that can bind-unbind to/from MT. We use the superscripts $i = \{KR, KL, FR, FL, c\}$ to represent the diverse dynein states. For instance, d^{KR} represents kinesin-bound right-moving dynein and d^{FL} represents free left-moving dynein. Cytoplasmic dynein density is denoted d^c.

We explored a number of assumptions about the transition between classes and the timescale of binding-unbinding, as well as rate of diffusion of dynein in the cytoplasm. These led to a hierarchy of distinct models at various levels of complexity. See schematic in **Fig. 3**B of the main text. We first discuss the boundary conditions and aspects shared by the models. Then we explain the distinct models and their predictions.

3.1 Boundary Conditions

As the MTs are unipolar and have plus ends at the cell tips, we assume no right-moving kinesin-bound dynein flux at $x = 0$. We also assume that total dynein is conserved, so that the boundary flux of the right-moving free dynein at $x = 0$ equals the sum of comet released dynein and the reflected flux of left-moving free dynein. Similar boundary conditions are applied at $x = L$. These assumptions lead to the following set of boundary conditions at the cell ends, implemented in each of the models we discuss:

$$\begin{aligned} vd^{KR}(0,t) &= 0, \quad vd^{KL}(L,t) = 0, \\ vd^{FR}(0,t) &= r^{rel}D^L + vd^{FL}(0,t), \\ vd^{FL}(L,t) &= r^{rel}D^R + vd^{FR}(L,t). \end{aligned} \tag{7}$$

The right and left ends of the cell have a distinct behaviour. Hence, we define the subpopulations $D^L(t)$ and $D^R(t)$ as the numbers of motors currently sequestered at the left and right ends, respectively. Their

time evolution is modeled as:

$$\begin{aligned} \frac{dD^R}{dt} &= vd^{KR}(L,t) - r^{rel}D^R, \\ \frac{dD^L}{dt} &= vd^{KL}(0,t) - r^{rel}D^L. \end{aligned} \quad [8]$$

where r^{rel} is the rate at which sequestered dynein is released to left- or right-moving dynein.

In cases where the diffusion of cytoplasmic dynein is considered, the boundary conditions used for d^c are

$$\begin{aligned} D\frac{\partial d^c}{\partial x}(0,t) &= 0, \\ D\frac{\partial d^c}{\partial x}(L,t) &= 0. \end{aligned} \quad [9]$$

We now explain the three distinct types of models and the various cases and submodels in each of these categories.

3.2 (i) Exchange only on single MT

We first considered the case that dynein and kinesin compete for dominance while walking along a single MT. In this case, when they exchange roles, their direction also switches (since kinesin walks towards the plus end while dynein walks to the minus end of a MT). The velocities of kinesin and dynein are not identical, but for simplicity, we use a single velocity v ($\sim 1.6\mu$m/s) for both in our models. We assumed that the motors remain on a single MT, and that binding-unbinding is negligeably small. Thus, in this model variant we could ignore the population of d^c and consider only four subpopulations of dynein, arriving at the set of equations

$$\begin{aligned} \frac{\partial d^{KR}}{\partial t} &= -v\tfrac{\partial d^{KR}}{\partial x} - r^{kf}d^{KR} + r^{fk}d^{FL}, \\ \frac{\partial d^{KL}}{\partial t} &= +v\tfrac{\partial d^{KL}}{\partial x} - r^{kf}d^{KL} + r^{fk}d^{FR}, \\ \frac{\partial d^{FR}}{\partial t} &= -v\tfrac{\partial d^{FR}}{\partial x} + r^{kf}d^{KL} - r^{fk}d^{FR}, \\ \frac{\partial d^{FL}}{\partial t} &= +v\tfrac{\partial d^{FL}}{\partial x} + r^{kf}d^{KR} - r^{fk}d^{FL}. \end{aligned}$$

Here r^{ij} are transition rates from state i to state j, and v is the motor velocity. The above consist of two pairs of coupled linear partial differential equations: d^{KR} is only coupled to d^{FL} and d^{KL} is only coupled to d^{FR}. Setting $\partial d^i/\partial t = 0$ leads to four ordinary differential equations for the spatial distributions that are easily solved explicitly.

Solving the steady state of above system with the boundary conditions [7], [8] we obtain the following solutions

$$d^{KR} = c_1 \frac{r^{fk}}{r^{kf}} \left(1 - e^{\frac{r^{fk}-r^{kf}}{v}x}\right), \qquad d^{FL} = c_1 \left(1 - \frac{r^{fk}}{r^{kf}} e^{\frac{r^{fk}-r^{kf}}{v}x}\right),$$
$$d^{KL} = c_1 \frac{r^{fk}}{r^{kf}} \left(1 - e^{\frac{r^{fk}-r^{kf}}{v}(L-x)}\right), \qquad d^{FR} = c_1 \left(1 - \frac{r^{fk}}{r^{kf}} e^{\frac{r^{fk}-r^{kf}}{v}(L-x)}\right),$$

where c_1 depends on the total amount of dynein whose mass is conserved. Using parameters from Table 1 in these expressions leads to the blue curve in Figure 3A of the main text. The dynein distribution predicted by this model predicts exponential decay near the two cell edges, and very low (exponentially decaying) dynein density in the bulk middle region.

3.3 (ii) Exchange through cytosol only

Here we assumed that dynein can only transition from MT bound to cytoplasmic, and from cytoplasmic to one of the four types $d^{KR}, d^{KL}, d^{FR}, d^{FL}$. This leads to the set of equations

$$\frac{\partial d^{KR}}{\partial t} = -v\frac{\partial d^{KR}}{\partial x} - r^{kc}d^{KR} + r^{ck}d^{c}, \qquad [10a]$$
$$\frac{\partial d^{KL}}{\partial t} = +v\frac{\partial d^{KL}}{\partial x} - r^{kc}d^{KL} + r^{ck}d^{c}, \qquad [10b]$$
$$\frac{\partial d^{FR}}{\partial t} = -v\frac{\partial d^{FR}}{\partial x} - r^{fc}d^{FR} + r^{cf}d^{c}, \qquad [10c]$$
$$\frac{\partial d^{FL}}{\partial t} = +v\frac{\partial d^{FL}}{\partial x} - r^{fc}d^{FL} + r^{cf}d^{c}. \qquad [10d]$$

We still need a fourth equation, for the cytoplasmic dynein d^c. There are two cases to consider, depending on whether the diffusion of dynein in the cytoplasm is rate limiting, or fast enough to render this subpopulation spatially uniform. Parameters for the exchange between MT and cytoplasm were estimated manually to produce a reasonable qualitative model behavior.

Case 1: Fast cytoplasmic diffusion

If the diffusion of d^c is very fast, then this cytoplasmic reservoir of dynein is spatially uniform, and its time evolution is governed by

$$\frac{dd^c}{dt} = \int_0^L -2(r^{cf} + r^{ck})d^c + r^{kc}d^{KR} + r^{kc}d^{KL} + r^{fc}d^{FL} + r^{fc}d^{FR}dx. \qquad [11]$$

Solving the steady state equations obtained by setting time derivatives to zero in Eqs. [10], [11] and using the boundary conditions [7], [8] and parameters from Table 1 leads to the steady state dynein

distribution shown in the left panel of Fig. 2. This distribution also has a biexponential shape, but minor difference between peak and trough density of dynein (only about 10% difference between the edge and bulk dynein densities).

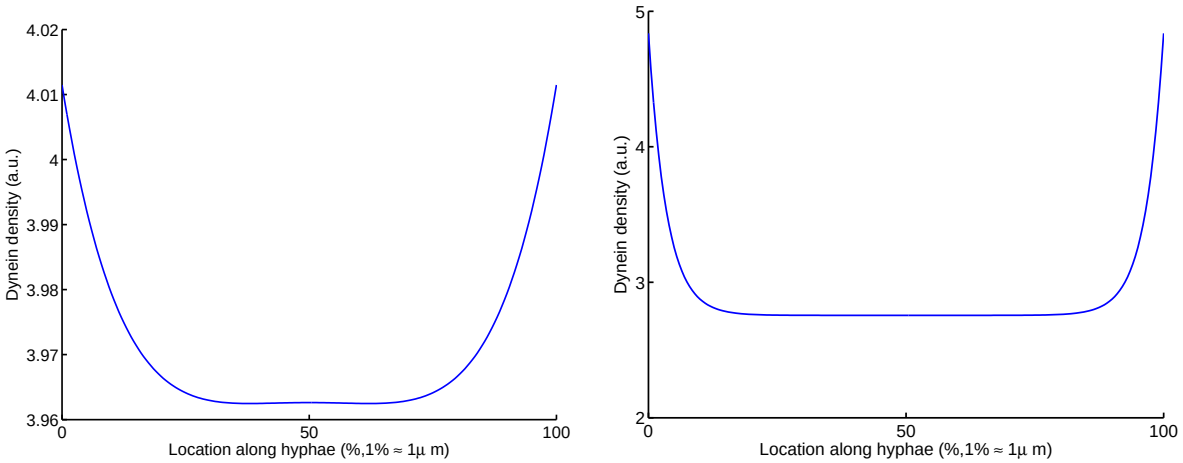

(a) **(b)**

Figure 2: Dynein distribution in Model (ii). Here dynein exchanges between MT-bound and cytoplasmic. (a) Rapidly diffusing cytoplasmic dynein (assumed spatially uniform). (b) Limited rate of cytoplasmic dynein diffusion.

Case (2): slow cytoplasmic diffusion

The importance of cytoplasmic diffusion can be quantified by the Peclet number, $Pe = vL/D$. The smaller the Peclet number, the larger the role of diffusion relative to advection as a means of transport of substances over space. In our case, $D = 10\mu m^2/s$ is a typical cytoplasmic diffusion coefficient for large biomolecules like dynein, and $v = 2\mu m/s$ is the approximate motor velocity. For dynamics on the length scale of the entire hyphae, $L = 100\mu m$ and $Pe \sim 20$ indicates that diffusion is negligible relative to motor velocity. However, we are concerned with dynamics in the tip regions with $L \sim 10\mu m \implies Pe \sim 2$, indicating that diffusion might be significant. To explore the consequences of diffusion, we replace Eqn. [11] with a full diffusion partial differential equation for d^c

$$\frac{dd^c}{dt} = D\frac{\partial^2 d^c}{\partial x^2} - 2(r^{cf} + r^{ck})d^c + r^{kc}d^{KR} + r^{kc}d^{KL} + r^{fc}d^{FL} + r^{fc}d^{FR}. \quad [12]$$

We use Eqs. [8] at the cell ends as before, and add [9] as boundary conditions on d^c. The system of steady state equations is solved on MatLab. Steady state solutions to this model are shown in the right panel of

Fig. 2. This model captures both the exponential decay at the cell edges and a sizable difference between dynein densities in the bulk and the cell edges.

3.4 (iii) Exchange between all states on MTs

Finally, we considered a model that represents both exchange between motors walking on the same MT and between adjoining MTs. There are many more state transitions to consider in this case. We assumed that there is a rate-limiting step (e.g., unbinding), followed by a rapid step (e.g. instantly rebinding to an available neighbouring MT). This avoids the need to track d^c in the model, reducing complexity to a more manageable level. However, the probability of rebinding to a right-facing MT (which determines the direction of motion once rebound) could, in principle, depend on the local MT array, captured by the fraction $P(x)$ computed earlier in Eqn. [5]. (The higher $P(x)$, the more likely a transition towards rebinding a right-facing MT.)

Incorporating the possible state transitions, the dynein dynamics is governed by the following system of PDEs:

$$\begin{aligned}
\frac{\partial d^{KR}}{\partial t} &= -v\tfrac{\partial d^{KR}}{\partial x} - (r^{KRKL} + r^{KRFR} + r^{KRFL})d^{KR} + r^{KLKR}d^{KL} + r^{FRKR}d^{FR} + r^{FLKR}d^{FL},\\
\frac{\partial d^{KL}}{\partial t} &= +v\tfrac{\partial d^{KL}}{\partial x} - (r^{KLKR} + r^{KLFR} + r^{KLFL})d^{KL} + r^{KRKL}d^{KR} + r^{FRKL}d^{FR} + r^{FLKL}d^{FL},\\
\frac{\partial d^{FR}}{\partial t} &= -v\tfrac{\partial d^{FR}}{\partial x} - (r^{FRKR} + r^{FRKL} + r^{FRFL})d^{FR} + r^{KRFR}d^{KR} + r^{KLFR}d^{KL} + r^{FLFR}d^{FL},\\
\frac{\partial d^{FL}}{\partial t} &= +v\tfrac{\partial d^{FL}}{\partial x} - (r^{FLKR} + r^{FLKL} + r^{FLFR})d^{FL} + r^{KRFL}d^{KR} + r^{KLFL}d^{KL} + r^{FRFL}d^{FR}.
\end{aligned}$$

About the parameters, we assumed

$$\begin{aligned}
&r^{KLKR} = r^{kk}P, \quad r^{KRKL} = r^{kk}(1-P), \quad r^{FLKL} = r^{fk}(1-P), \quad r^{FRKL} = r^{fk},\\
&r^{KLFL} = r^{kf}P, \quad r^{KRFL} = r^{kf}, \quad r^{FLKR} = r^{fk}, \quad r^{FRKR} = r^{fk}P,\\
&r^{KLFR} = r^{kf}, \quad r^{KRFR} = r^{kf}(1-P), \quad r^{FLFR} = r^{ff}(1-P), \quad r^{FRFL} = r^{ff}P.
\end{aligned}$$

We assumed that $P = P(x)$ is the fraction of right facing MT computed in [5] in the MT nucleation model. A representative result is shown in the red curve in Fig. 3A of the main text and in (Supplement) Fig. 3.

For some parameter values ($r^{fk} = 0.1$/s, $r^{kf} = 0.01$/s, $r^{kk} = 0.3$/s, $r^{ff} = 1$/s, $r^{rel} = 0.1$/s and $v = 1.6\mu$m/s), the dynein distribution can develop multiple peaks and troughs, similar to the underlying MT polarity array distribution. We show the total dynein density by the black curve in Fig. 3(a). By decomposing this total into its four component motor subpopulations (same figure), we find that the bump occurs in free dynein ($d^{FR,FL}$). These bumps result from the discontinuity of the right/left facing MT

density at $x = 10\mu$m and 90μm shown in (Supplement) Fig. 1(B)vii (equivalent to Fig 2G of the main text). The key to making this bump appear turns out to be decreasing the difference $r^{fk} - r^{kf}$ relative to parameters listed in the table. A similar dynein distribution occurs for $r^{fk} = 0.3$/s, $r^{kf} = 0.2$/s, $r^{kk} = 1$/s, $r^{ff} = 1$/s, but with a less prominent bump and lower differences between cell ends and cell center. Keeping other parameters unchanged and setting $r^{kk} = 1$/s, $r^{ff} = 0.3$/s leads to loss of the bump, as shown in Fig. 3(b).

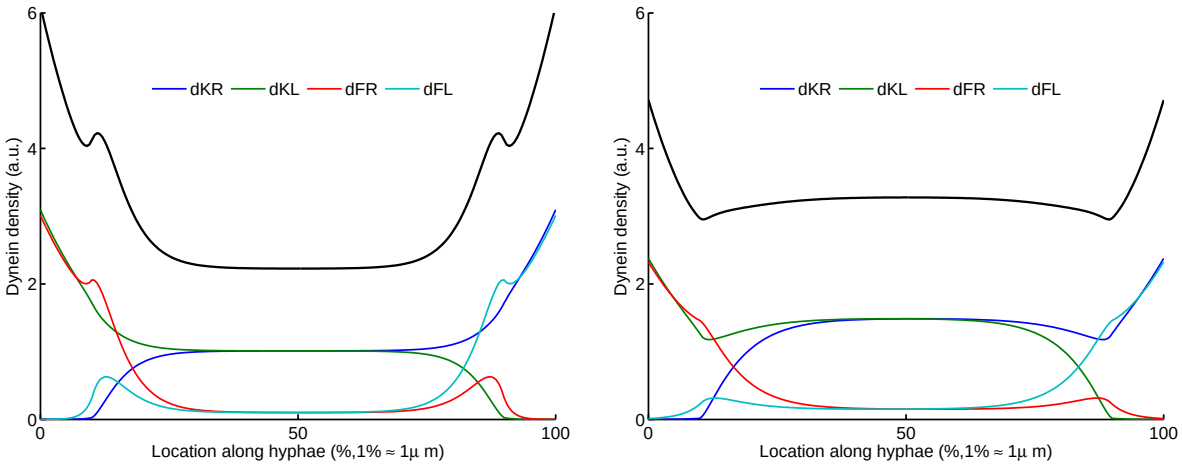

(a) **(b)**

Figure 3: Dynein Model (iii) includes transitions between all states, with a rapid rebinding. Parameters used in this model are (a) $r^{fk} = 0.1$/s, $r^{kf} = 0.01$/s, $r^{kk} = 0.3$/s, $r^{ff} = 1$/s, $r^{rel} = 0.1$/s and $v = 1.6\mu$m/s; a bump is evident in the dynein distribution. (b) $r^{kk} = 1$/s, $r^{ff} = 0.3$/s (with other parameters as before); loss of the bump in the total dynein.

We investigated how the microtubule length affects the results shown in Fig. 3(a). As before, we considered cases with a halved and a doubled value of the MT catastrophe rate, k_c. Results are shown in Fig 4. It is evident that the resultant dynein distributions are highly similar, with a slight displacement of the bump, and minor ($< 10\%$) change in the background mid-cell level.

4 Early endosome (EE) Dynamics

Let u^i represent the density of early endosomes (EE) in state i, where $i \in \{KR, KL, DR, DL\}$. For instance, u^{KR} and u^{DL} are the densities of right-moving kinesin-attached and left-moving dynein-attached

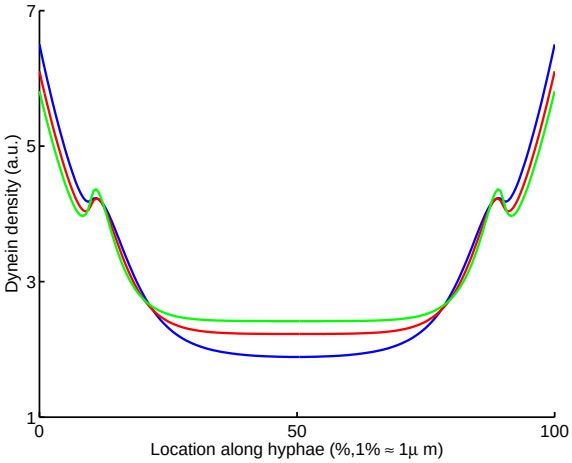

Figure 4: Effect of changing the mean MT length on the dynein distribution. Red curve — reported catastrophe rate ($k_c = 2.4\text{min}^{-1}$); blue curve — half catastrophe (longer MTs); green curve — double catastrophe rate (shorter MTs).

endosomes, respectively. The transitions between EE subpopulations are shown in Figure 1B of the main text. There are many transitions, and formally, the structure of the model is as follows:

$$\frac{\partial u^{KR}}{\partial t} = -v^{KR}\frac{\partial u^{KR}}{\partial x} - (f^{KRKL} + f^{KRDL} + f^{KRDR})u^{KR} + f^{KLKR}u^{KL} + f^{DRKR}u^{DR} + f^{DLKR}u^{DL},$$
$$\frac{\partial u^{KL}}{\partial t} = +v^{KL}\frac{\partial u^{KL}}{\partial x} + f^{KRKL}u^{KR} - (f^{KLKR} + f^{KLDR} + f^{KLDL})u^{KL} + f^{DRKL}u^{DR} + f^{DLKL}u^{DL},$$
$$\frac{\partial u^{DR}}{\partial t} = -v^{DR}\frac{\partial u^{DR}}{\partial x} + f^{KRDR}u^{KR} + f^{KLDR}u^{KL} - (f^{DRDL} + f^{DRKL} + f^{DRKR})u^{DR} + f^{DLDR}u^{DL},$$
$$\frac{\partial u^{DL}}{\partial t} = +v^{DL}\frac{\partial u^{DL}}{\partial x} + f^{KRDL}u^{KR} + f^{KLDL}u^{KL} + f^{DRDL}u^{DR} - (f^{DLDR} + f^{DLKL} + f^{DLKR})u^{DL}.$$

Here, for instance, f^{KLKR} represents the transition rate from kinesin-bound left-moving EE to kinesin-bound right-moving EE. We must now specify the nature of the transition rates f^i that we are assuming.

We model transitions between EE states as competing Poisson processes and make two assumptions: (1) the transition rate from any state into a dynein-driven state is proportional to the local concentration of dynein. (Since kinesin-3 is constitutively loaded onto the EE (4), the transition rate into a kinesin-driven state is constant); and (2) the transition rate onto a left-facing (respectively right-facing) MT is proportional to the fraction of left-facing (respectively right-facing) MTs at that location.

Our model is deliberately agnostic about the molecular mechanism that drives these transition events. However, we note that the two above assumptions arise naturally in a stochastic tug-of-war model of

cargo switching. They are also the most natural assumptions in a regulated switching model, since any alternative transition rates would imply a bias towards a subset of MTs or a subset within a species motors, and would thus require a further upstream mechanism to explain that bias. Given this motivation, we used the following forms for the transition rates:

$$\begin{aligned}
&f^{KLKR} = r^0 P, && f^{KLDL} = r^0 P\frac{d}{d_0}, && f^{KLDR} = r^0\frac{d}{d_0},\\
&f^{KRKL} = r^0(1-P), && f^{KRDL} = r^0\frac{d}{d_0}, && f^{KRDR} = r^0(1-P)\frac{d}{d_0},\\
&f^{DLKL} = r^1(1-P), && f^{DLKR} = r^1, && f^{DLDR} = r^1(1-P)\frac{d}{d_0},\\
&f^{DRKL} = r^1, && f^{DRKR} = r^1 P, && f^{DRDL} = r^1 P\frac{d}{d_0}.
\end{aligned}$$

Here, d_0 is the local concentration of dynein at which transitions to dynein-driven states are equally likely as transitions to kinesin-driven states. The parameters r^0 and r^1 are the basal transition rates out of a kinesin-driven or, respectively, dynein-driven state in the absence of available dynein, $d(x)$ is the local dynein concentration, and $P(x)$ is the MT array polarity. Many of the above parameters are thus spatially dependent.

The boundary conditions for this system are

$$\begin{aligned}
&v^{KR}u^{KR}(0,t) = 0, \qquad v^{KL}u^{KL}(L,t) = 0,\\
&v^{DR}u^{DR}(0,t) = v^{KL}u^{KL}(0,t) + v^{DL}u^{DL}(0,t),\\
&v^{DL}u^{DL}(L,t) = v^{KR}u^{KR}(L,t) + v^{DR}u^{DR}(L,t).
\end{aligned}$$

As before, we assume no right-moving kinesin-bound EE flux at $x = 0$. Assuming the total EE is conserved, the boundary flux of the right-moving dynein-bound EE at $x = 0$ equals the sum of the left-moving kinesin-bound EE flux and the reflected flux of left-moving dynein-bound EE. Similar boundary conditions are applied at $x = L$.

Results of this WT model are shown in Figure 4 of the main text. We also reran this model for longer and shorter MT by halving and doubling the catastrophe rate k_c. Results were practically indistinguishable, and are omitted for brevity.

To calculate the run length, we use an initial condition with a non-zero value restricted to one edge and simulate the transport by right-moving motors. We set $v^{DL} = 0$ and $v^{KL} = 0$ so that EEs attaching to a left-moving motor get frozen at their current location. This results in a distribution of EEs along the cell length which we can interpret as the probability distribution of the distance travelled by an EE before switching direction. The histogram in the main text (Fig 5) is obtained by counting the number of EEs in every $10\mu m$ of the simulated cell.

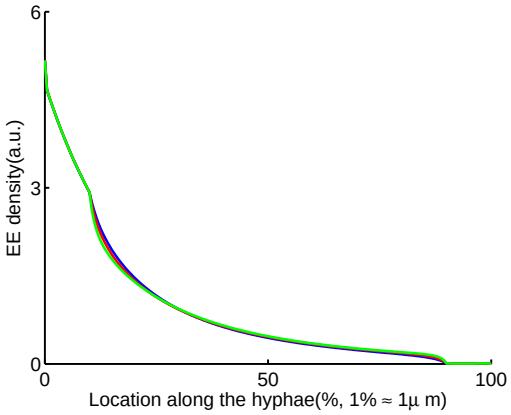

Figure 5: Effect of changing the mean MT length on the run length distribution. Red curve — reported catastrophe rate ($k_c = 2.4\text{min}^{-1}$); blue curve — half catastrophe (longer MTs); green curve — double catastrophe rate (shorter MTs). Note that the curves are practically identical.

For longer and shorter MTs (k_c halved and doubled) we obtain highly similar run lengths, as shown in Fig 5.

5 Parameter Estimation

Parameter values were estimated from the literature as described below. Table 1 summarizes the values we used with the source on which they are based.

Parameters for the microtubule model have been well-established in previous theoretical and experimental papers, and are drawn from the classic literature on that subject cited in Table 1. The nucleation rate for MT, k_{nuc0} depends on local levels of γ-tubulin and the tubulin dimer level, which are not explicitly considered in our model. We model nucleation implicitly by choosing k_{nuc0} to match the model prediction for the MT plus ends distribution to data shown in Figure 1C in the paper (4). Equivalently, it can also be estimated from the total number of microtubules in a cross-section of the cell, $N(x)$.

For the dynein model we adopted the simplest model with dynein-kinesin exchange while walking on a single microtubule, no unbinding from the MT, and no significant rebinding of freely diffusing particles (Model (i)). This simplification means that there are only two exchange rate parameters (from kinesin to dynein walking, r^{kf} and from dynein to kinesin walking r^{fk}). This simple model is analytically solvable, and results in a prediction for the spatial decay length $v/(r^{fk} - r^{kf})$ of the exponential dynein distribution. We fit this value to the approximate observed spatial scale for the dynein comet distribution in Figure 3D

Table 1: Parameter Used

	Parameters	Definitions	Values	Units	Source
MT model	L	length of cell	100	μm	(3)
	l_{nuc}	"size" of cell tips(no nucleation region)	10	μm	(4)
	v_g	MTs growing rate	11	μm/min	(5)
	v_s	MTs shrinking rate	37	μm/min	(5)
	k_{nuc0}	MTs nucleation rate	1	$\mu m^{-1}\text{min}^{-1}$	Estimated
	k_r	transition rate from growing to shrinking	0.44	min^{-1}	(5)
	k_c	transition rate from shrinking to growing	2.4	min^{-1}	(5)
Dynein Model	r^{kf}	transition rate from kinesin bound to free dynein	0.3	s^{-1}	Estimated
	r^{fk}	transition rate of free to kinesin bound dynein	0.5	s^{-1}	Estimated
	v	dynein velocity	1.6	$\mu m/s$	(3)
	r^{rel}	comet dynein releasing rate	0.1	s^{-1}	(3)
EE model	r^0	detachment rate of kinesin-bound EE	0.1	s^{-1}	Estimated
	r^1	detachment rate of dynein-bound EE	0.08	s^{-1}	Estimated
	v^{KR}	velocity of right-moving kinesin-EE	2	$\mu m/s$	(4)
	v^{KL}	velocity of left-moving kinesin-EE	2	$\mu m/s$	(4)
	v^{DR}	velocity of right-moving dynein-EE	1.7	$\mu m/s$	(3)
	v^{DL}	velocity of left-moving dynein-EE	1.7	$\mu m/s$	(3)

in the paper (2). The dynein velocity and comet release rate are both taken from experimental literature. We adjusted the absolute value of the parameters r^{fk}, r^{kf} manually for a preliminary fit, and refined this adjustment in the last model phase.

For the endosome model, the velocity parameters $v^{KR,KL}, v^{DR,DL}$ are known, and we had to estimate r^0, r^1. To do so, we fitted the model to data for the run length distribution (Figure 3B) in (4). At this stage, small refinement was made to r^{fk}, r^{kf} for the optimal model fit.

6 Mutants

For the dynein and kinesin mutant simulations, we assumed that the respective motors can still bind to EEs but are not functional anymore, i.e. that in the mutant, the given motor does not move. Hence $v^{DR} = 0$, $v^{DL} = 0$ in the dynein mutant and set $v^{KR} = 0$, $v^{KL} = 0$ in the kinesin mutant.

References

1. Marileen Dogterom and Stanislas Leibler. Physical aspects of the growth and regulation of microtubule structures. *Physical review letters*, 70(9):1347, 1993.

2. J H Lenz, I Schuchardt, A Straube, and G Steinberg. A dynein loading zone for retrograde endosome motility at microtubule plus-ends. *EMBO Journal*, 25(11):2275–2286, 2006.

3. Martin Schuster, Sreedhar Kilaru, Peter Ashwin, Congping Lin, Nicholas J Severs, and Gero Steinberg. Controlled and stochastic retention concentrates dynein at microtubule ends to keep endosomes on track. *The EMBO Journal*, 30(4):652–664, 2011.

4. Martin Schuster, Sreedhar Kilaru, Gero Fink, Jérôme Collemare, Yvonne Roger, and Fred Chang. Kinesin-3 and dynein cooperate in long-range retrograde endosome motility along a nonuniform microtubule array. *Molecular Biology of the Cell*, 22:3645–3657, 2011.

5. Gero Steinberg, R Wedlich-Soldner, Marianne Brill, and Irene Schulz. Microtubules in the fungal pathogen Ustilago maydis are highly dynamic and determine cell polarity. *Journal of cell science*, 114(3):609–622, 2001.